Electronic Supplementary Material (ESI) for Journal of Materials Chemistry

Planar Ni(II), Cu(II) and Co(II) Tetraaza[14]annulenes: Structural, Electronic and Magnetic Properties and Application to Field Effect Transistors

Alexander M. Whyte,[a] Yoshiaki Shuku,[b] Gary S. Nichol,[a] Michio Matsushita,[b] Kunio Awaga,[b] and Neil Robertson*[a]

Received (in XXX, XXX) Xth XXXXXXXXX 20XX, Accepted Xth XXXXXXXXX 20XX

DOI: 10.1039/b000000x

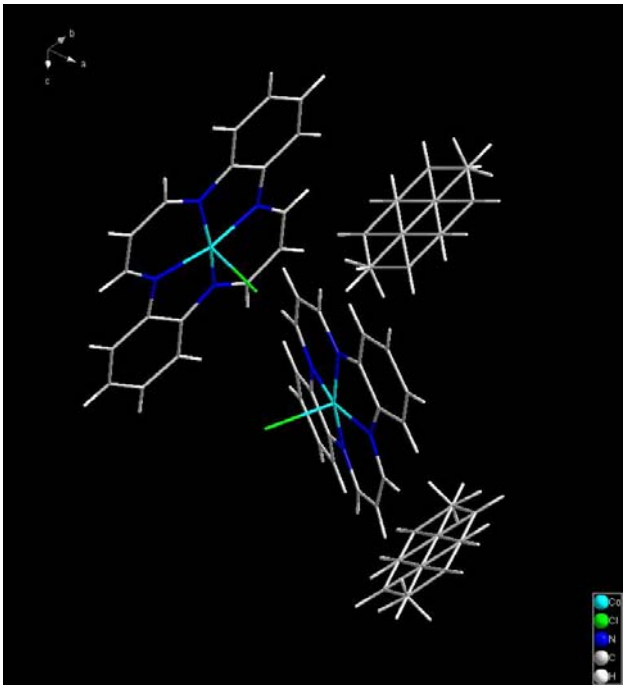

Figure S1 Crystal structure of Co(L1)(Cl) in the presence of disordered toluene.

Table 1 Crystallographic information for Cu(L1), Ni(L2) and Co(L1)Cl.toluene.

Complex	Co(L1)	Cu(L1)	Ni(L2)	Co(L1)Cl.toluene
Morphology	Black needle (0.18 × 0.03 × 0.01 mm)	Red prism (0.12 x 0.09 x 0.04 mm)	Red prism (0.06 x 0.05 x 0.04 mm)	Black block (0.25 x 0.11 x 0.06)
Empirical formula	$C_{18}H_{14}CoN_4$	$C_{18}H_{14}CuN_4$	$C_{26}H_{18}N_4Ni$	$C_{43}H_{36}Cl_2Co_2N_8$
T (K)	100	150.1	150.1	100
Space group	$Pna2_1$	$P2_1/c$	$Cmc2_1$	P -1
M_r	345.26	349.88	445.15	853.58
a	14.707(2)	19.416(5)	20.428(4)	9.3850(9)

b	5.1858(8)	5.1511(12)	12.905(2)	13.3040(12)
c	17.973(3)	14.878(4)	6.9730(12)	15.3654(11)
α	90	90.00	90.00	74.895(7)
β	90	112.394(3)	90.00	81.155(7)
γ	90	90.00	90.00	75.541(8)
V	1370.8(4)	1375.8(6)	1838.3(6)	1785.5(3)
D_c	1.673	1.689	1.608	1.59
μ	1.256	1.592	1.079	9.023
No. of reflections measured	7681	10218	7216	34656
No. of reflections used	1461	3454	2063	6975
θ_{max}	20.66	27.5	27.48	72.96
Z	4	2	4	2
R_{int}	0.0964	0.048	0.035	0.101
T_{min}/T_{max}	0.8055/0.9875	0.866/ 0.938	0.892/0.958	0.32/0.58
R_1 (I > 2σ(I))	0.0535	0.0364	0.0377	0.0833
wR (F^2) (I > 2σ(I))	0.1272	0.1050	0.0962	0.0728

Table S2 Selected bond lengths and angles of Co(L1), Co(L1).Cl, Cu(L1) and Ni(L2).

Bond length / Angle	Co(L1)	Co(L1).Cl	Cu(L1)	Ni(L2)
M1-N (Å)	1.896(11), 1.886(10) 1.836(11), 1.870(10)	1.887(3), 1.887(2) 1.893(4), 1.881(2)	1.926(2), 1.927(2)	1.866(2), 1.865(2)
M2-N (Å)	-	1.885(3), 1.895(3) 1.899(3), 1.889(2)	1.927(2), 1.928(1)	-
N-M1-N (°)	84.7(7), 87.0(6)	84.4(1), 84.0(1)	84.50(7)	84.98(9)
N-M1-N' (°)	92.8(6), 95.4(7)	94.5(1), 93.9(1)	95.50(7)	95.07(9)
N-M2-N (°)	-	83.7(1), 84.1(1)	84.53 (7)	-
N-M2-N' (°)	-	94.4(1), 94.6(1)	95.47(7)	-
N···N bite distance (Å)	2.55(2), 2.55(2)	2.535(4), 2.526(4)	2.591(2), 2.593(1)	2.520(3)

		2.539(4), 2.523(4)		
N···N' distance (Å)	2.70(2), 2.79(2)	2.766(4), 2.762(4) 2.770(4), 2.789(4)	2.852(3), 2.853 (2)	2.752(3)

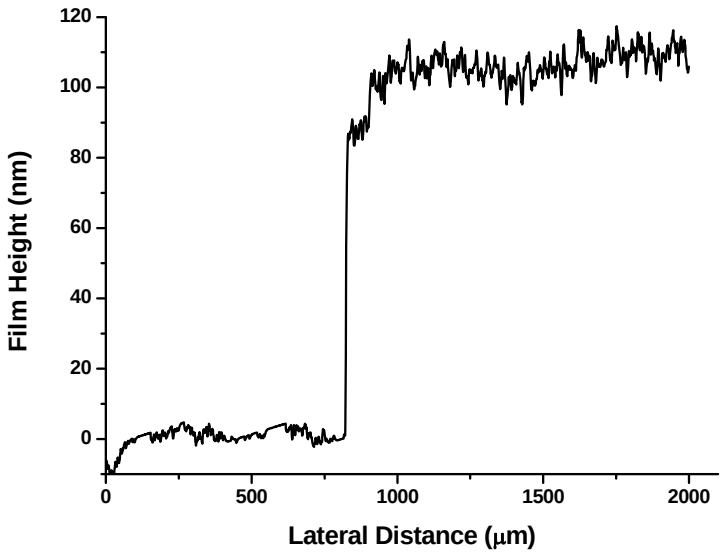

Figure S2 Profile of Ni(L1) showing a film thickness of approximately 100 nm.

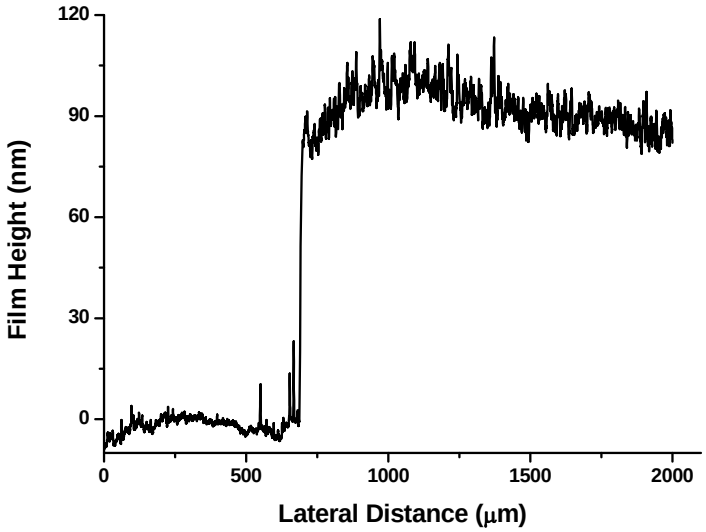

Figure S3 Profile of Co(L1) showing a film thickness of approximately 90 nm.

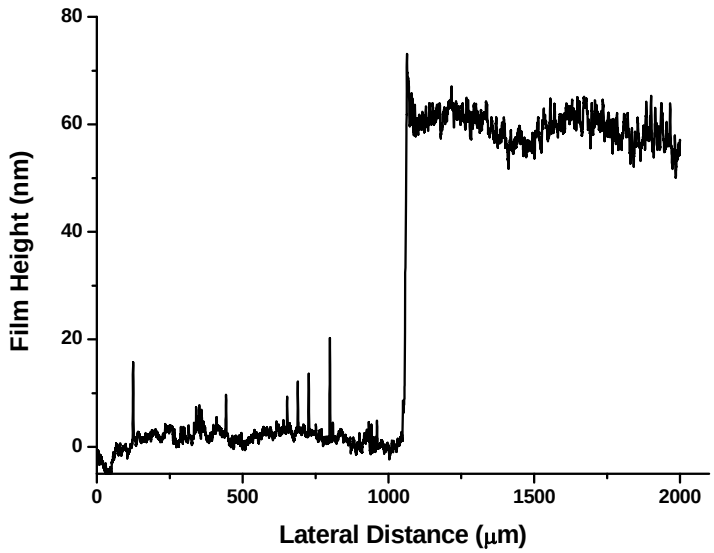

Figure S4 Profile of Cu(L1) showing a film thickness of approximately 60 nm.

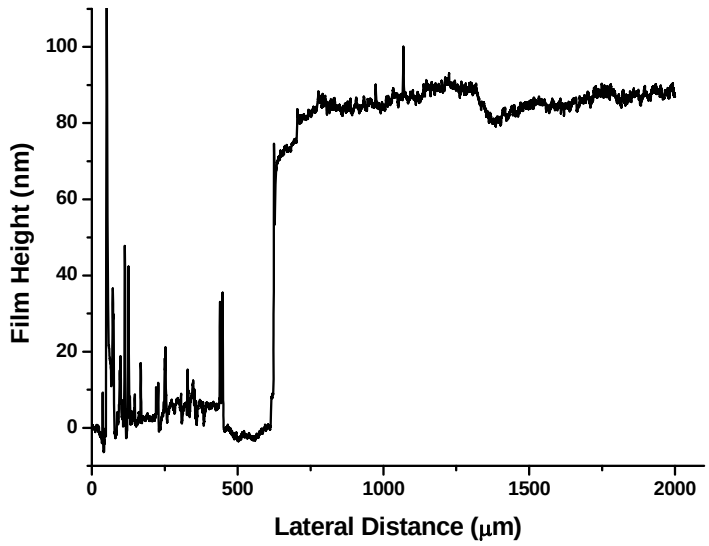

Figure S5 Profile of Ni(L2) showing a film thickness of approximately 90 nm.

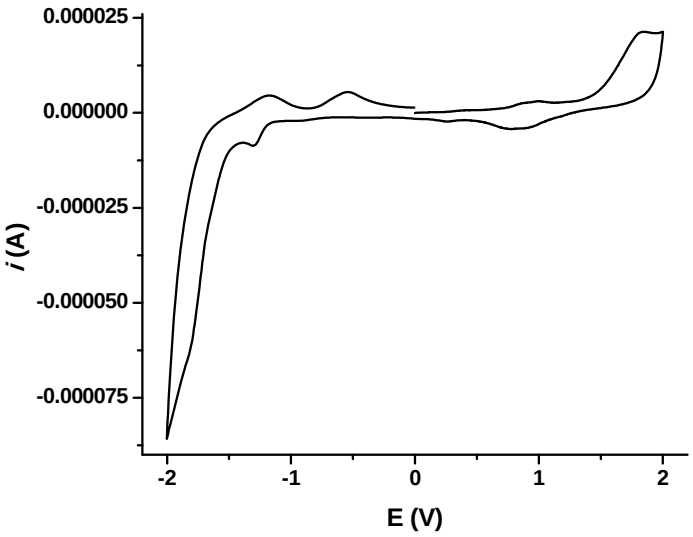

Figure S6 Cyclic voltammagram of Co(L1) in 0.3M $TBAPF_6$/DCM at a scan rate of 0.1 V/s.

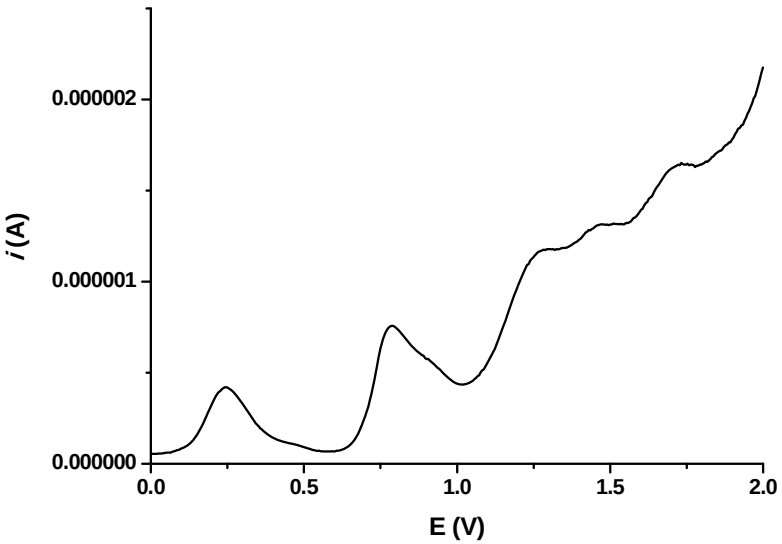

Figure S7 Differential pulse voltammogram of Co(L1) in 0.3M $TBAPF_6$/DCM scanning from 0 to 2 V.

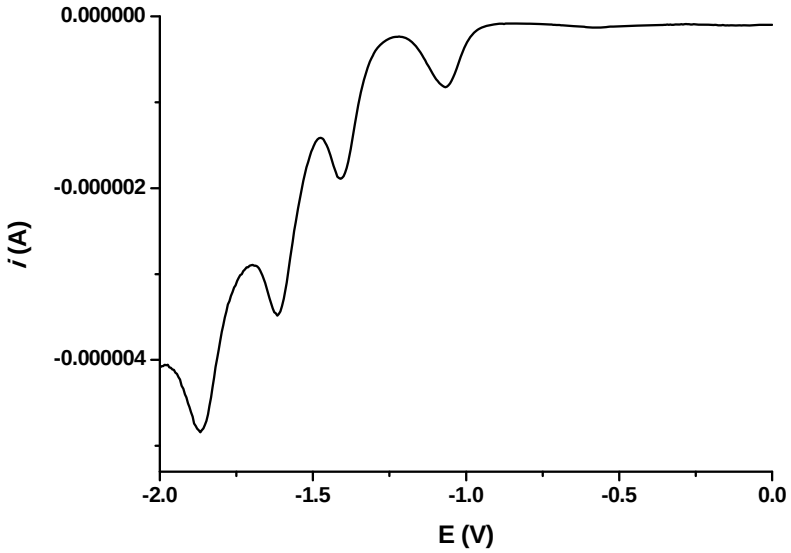

Figure S8 Differential pulse voltammogram of Co(L1) in 0.3M $TBAPF_6$/DCM scanning from 0 to -2 V.

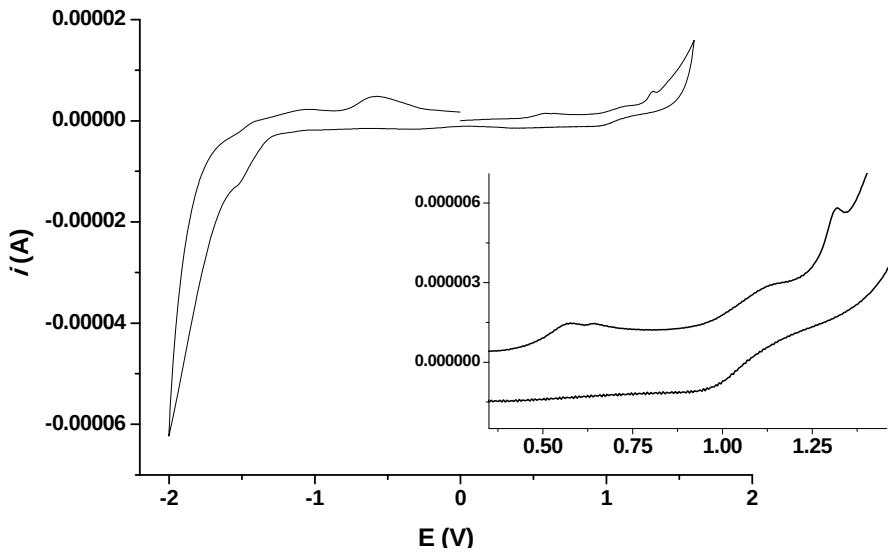

Figure S9 Cyclic voltammetry of Cu(L1) in 0.3M $TBAPF_6$/DCM. The CV is hampered by the material's poor solubility but a reduction peak at -1.51 V and three oxidation processes (inset) at 0.58, 1.12 and 1.32 V are just visible in broad agreement with the differential pulse results.

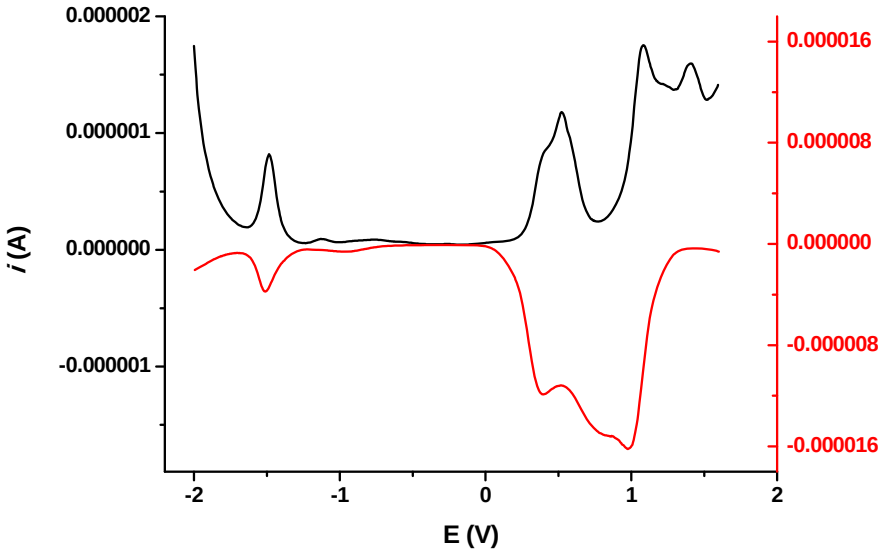

Figure S10 Differential pulse voltammogram of Cu(L1) in 0.3M $TBAPF_6$/DCM.

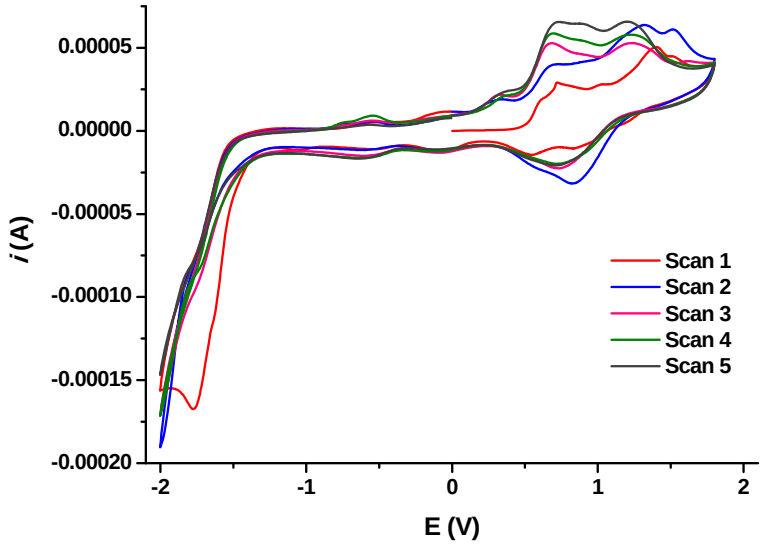

Figure S11 Cyclic voltammetry of Ni(L1). Five scans were carried out starting from 0 V, sweeping to 2 V then to –2 V, before returning to the initial starting point.

Figure S12 The Pt working electrode before (left) and after (right) scanning 5x between 2 and -2 V.

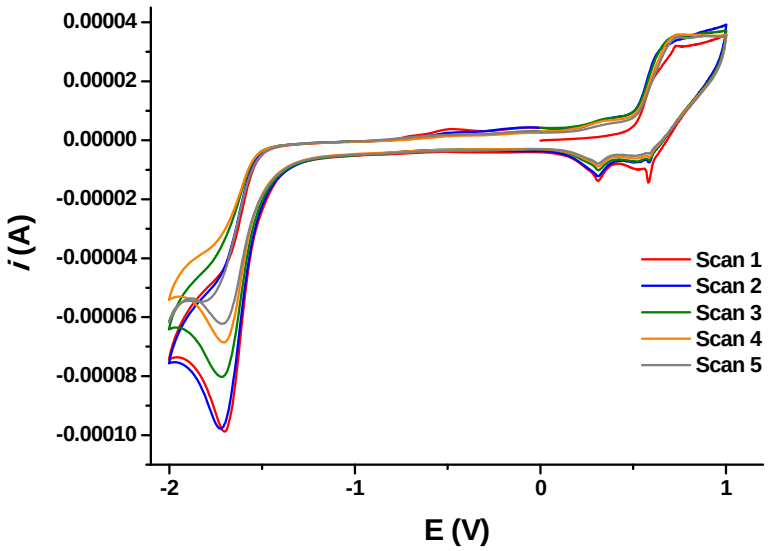

Figure S13 Cyclic voltammetry of Ni(L1). Five scans were carried out starting from 0 V, sweeping to 1 V then to –2 V, before returning to the initial starting point.

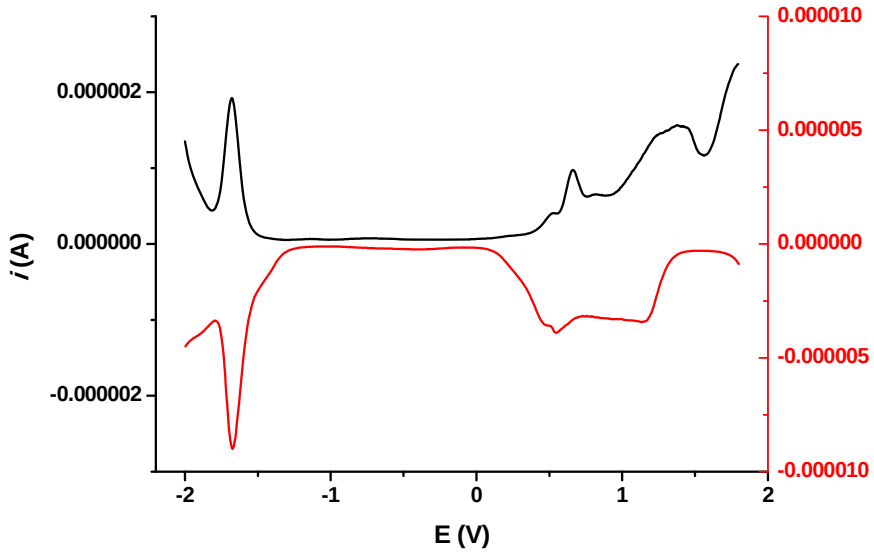

Figure S14 Differential pulse voltammogram of of Ni(L1) in 0.3M $TBAPF_6$/DCM.

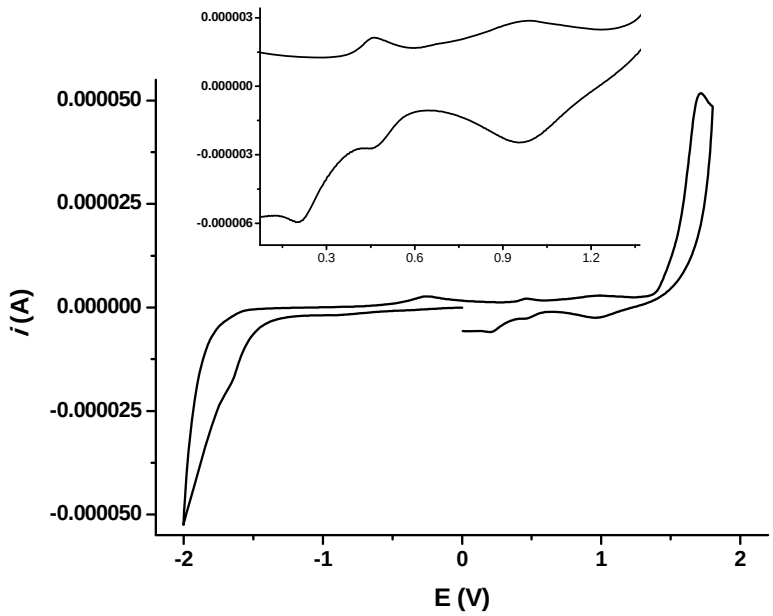

Figure S15 Cyclic voltammagram of Ni(L2) in 0.3M $TBAPF_6$/DCM at a scan rate of 0.1 V/s.

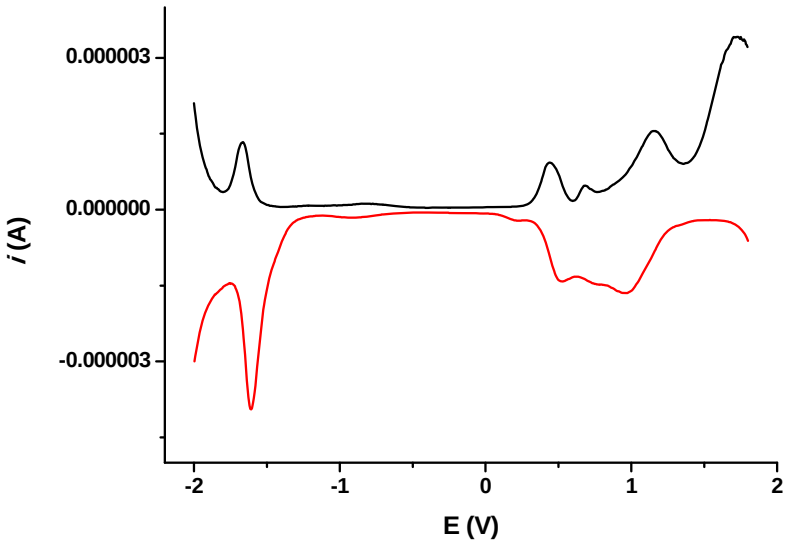

Figure S16 Differential pulse of Ni(L2) in 0.3M $TBAPF_6$/DCM.

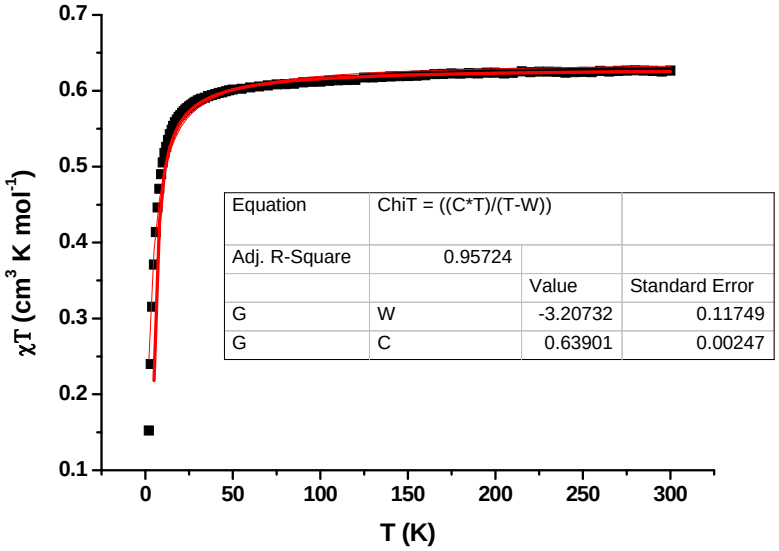

Figure S17 χT vs. T plot of Co(L1) fit to the Curie Weiss law. The red line shows the fit to the experimental data in black.

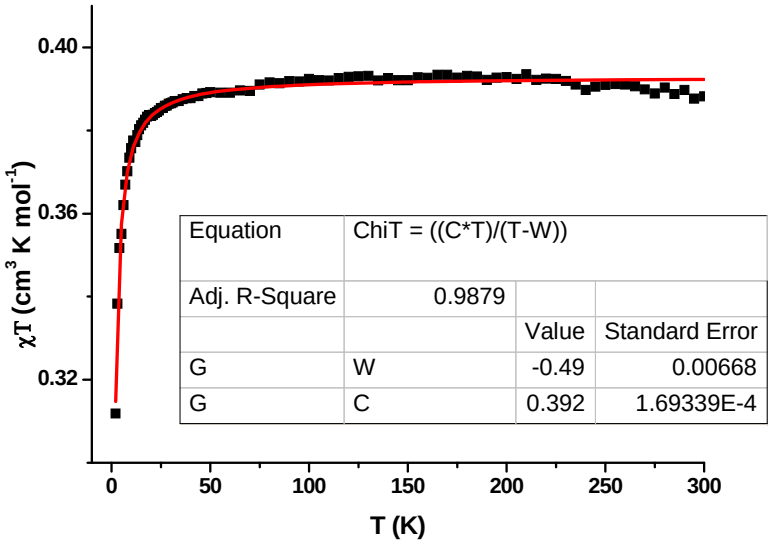

Figure S18 χT vs. T plot of Cu(L1) fit to the Curie Weiss law. The red line shows the fit to the experimental data in black.

Optimised Geometry:

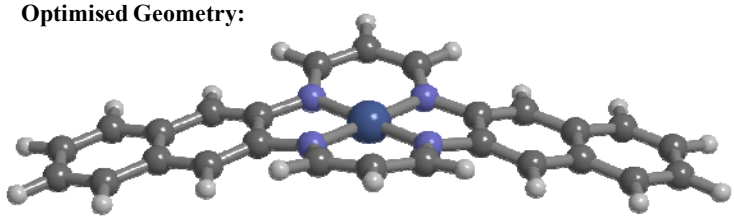

Crystallised Geometry:

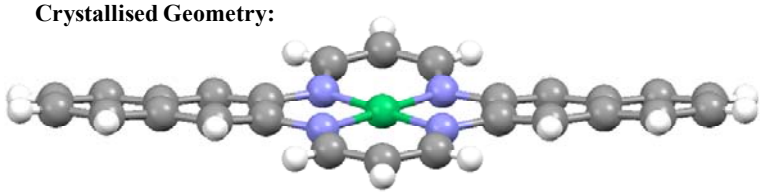

Figure S19 Comparison of structure obtained from geometry optimisation calculation versus the structure obtained from single crystal diffraction.

Table S3 Ni(L1) and Ni(L2) molecular orbitals generated from DFT calculations at the B3LYP/6-31G level of theory with the orbital energy in volts underneath.

Orbital	Ni(L1)	Ni(L2)

LUMO+2	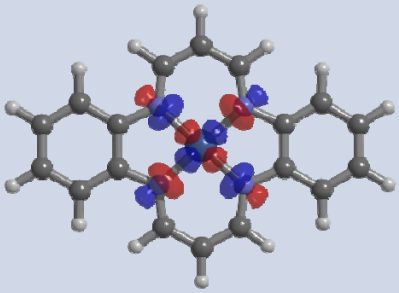 **-0.57**	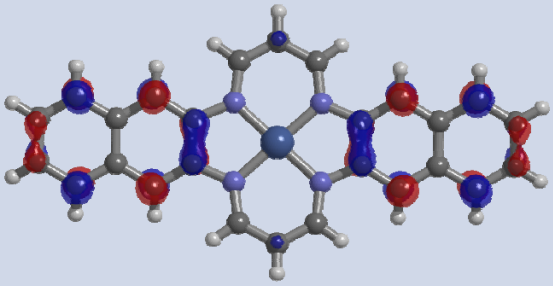 **-0.73**
LUMO+1	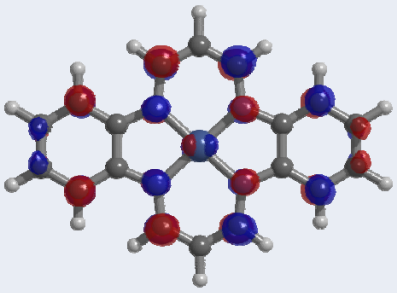 **-1.27**	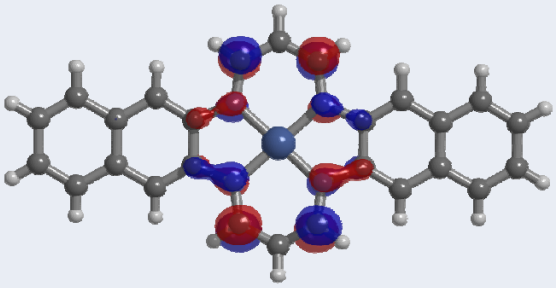 **-1.67**
LUMO	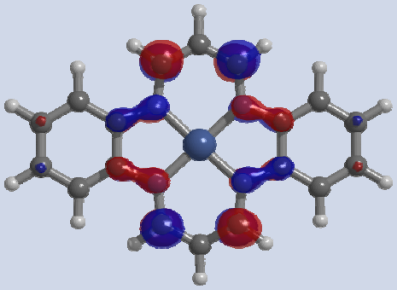 **-1.70**	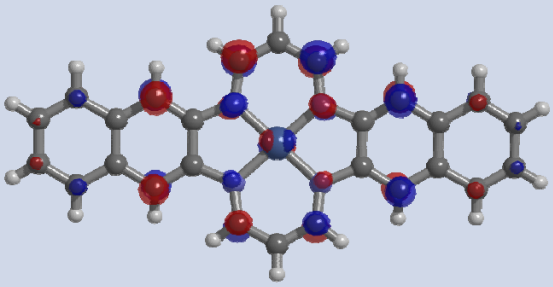 **-1.72**
HOMO	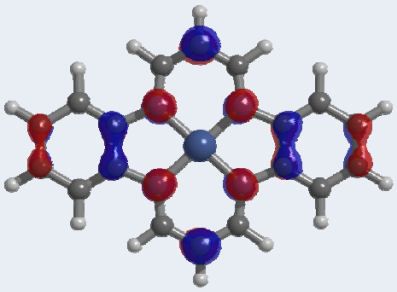 **-4.85**	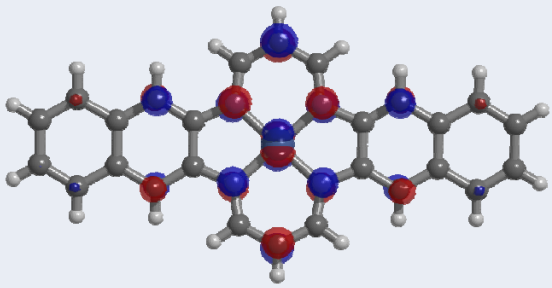 **-4.79**

HOMO-1	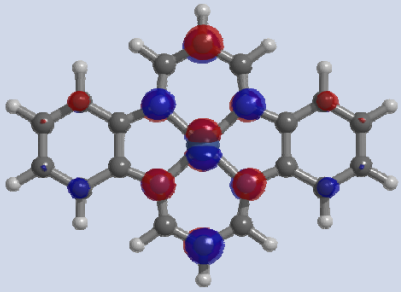 **-5.12**	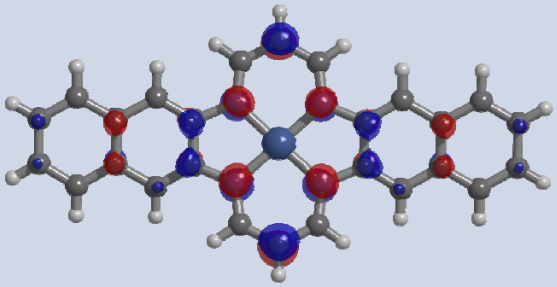 **-4.98**
HOMO-2	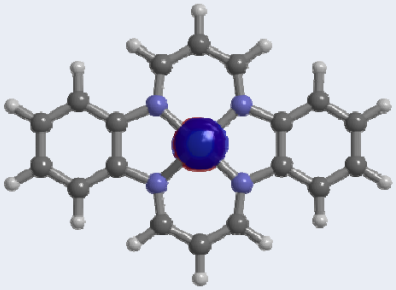 **-5.89**	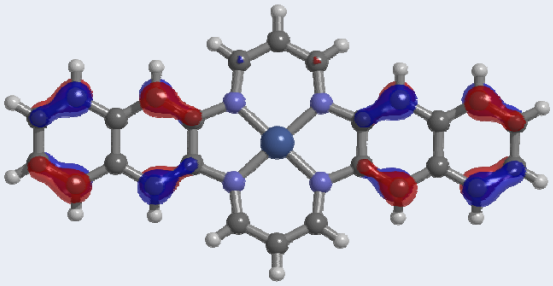 **-5.68**
HOMO-3	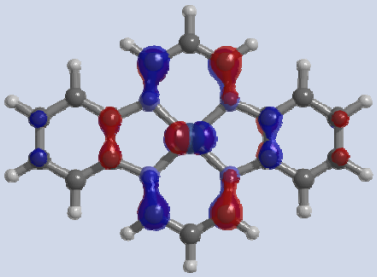 **-5.95**	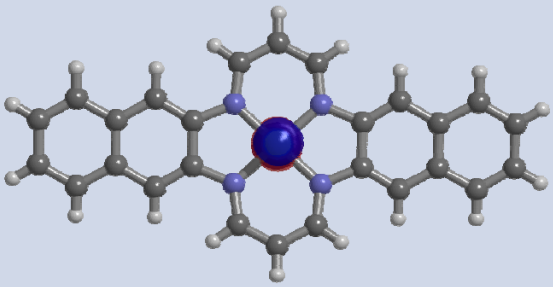 **-5.83**
HOMO-4	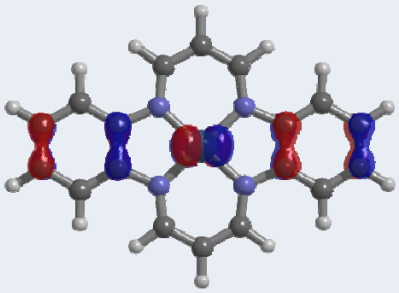 **-6.54**	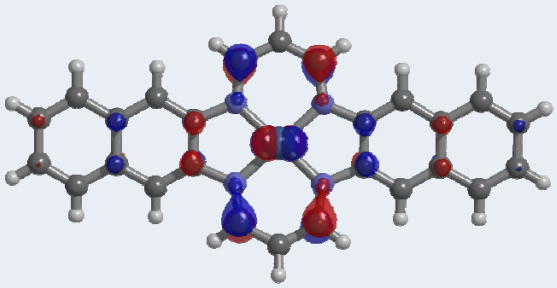 **-5.91**

HOMO-5	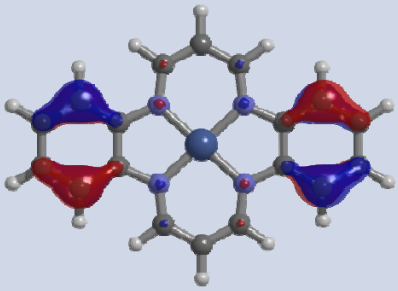 **-6.59**	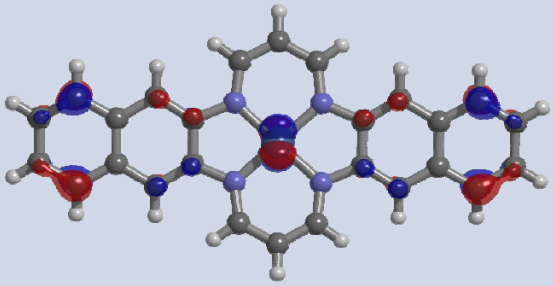 **-6.11**
HOMO-6	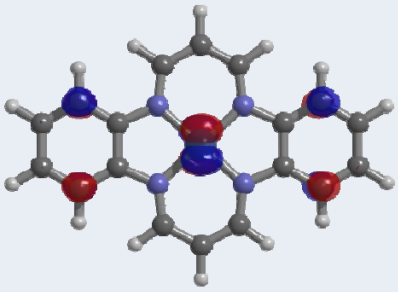 **-6.76**	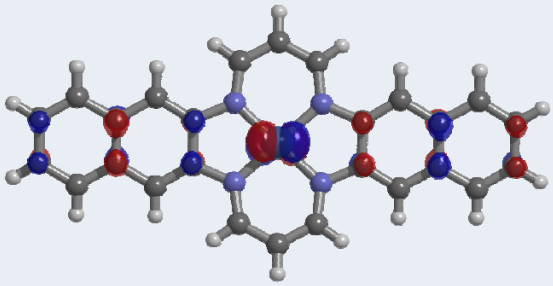 **-6.35**

Table S4 Co(L1) orbitals and energies from single point calculations at the B3LYP/6-31G(d,p) level of theory

Orbital	Alpha electron	Beta electron
LUMO+2	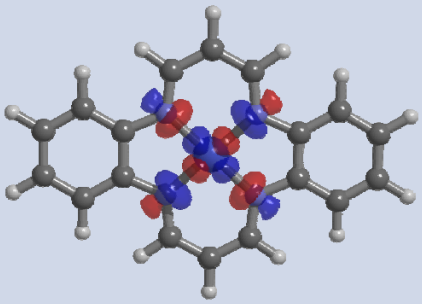 **-0.23**	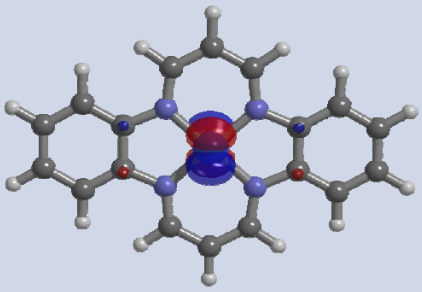 **-1.04**

LUMO+1	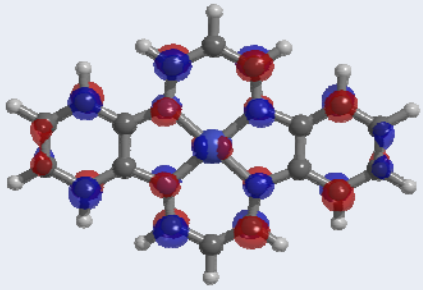 **-1.22**	 **-1.15**
LUMO	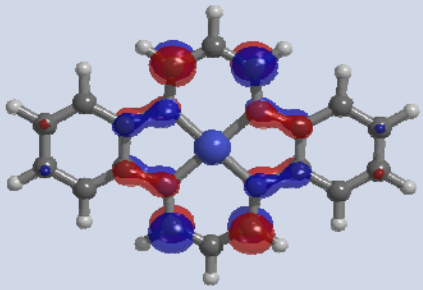 **-1.67**	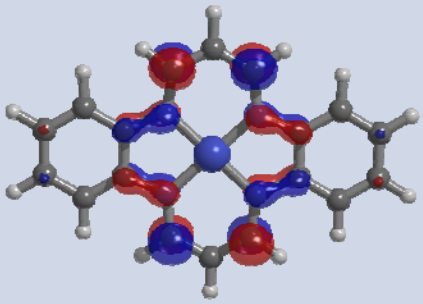 **-1.70**
HOMO	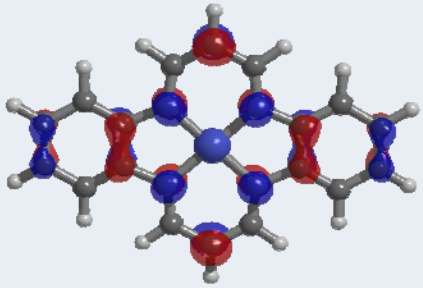 **-4.84**	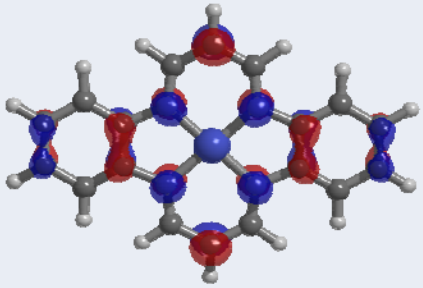 **-4.81**
HOMO-1	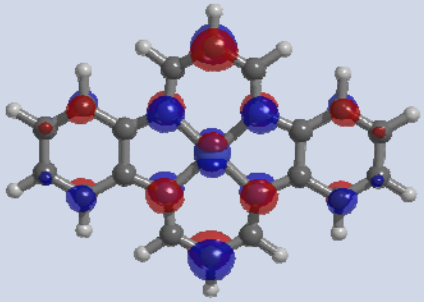 **-5.37**	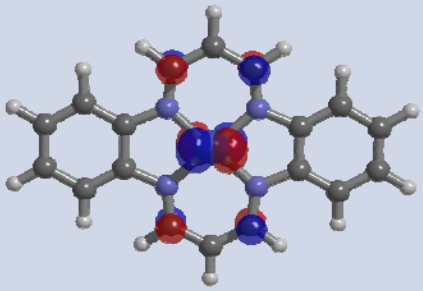 **-5.27**

HOMO-2	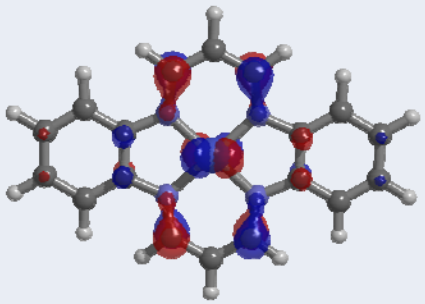 **-5.84**	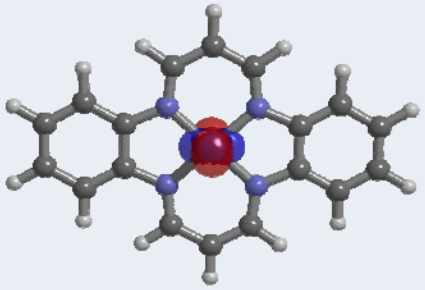 **-5.48**
HOMO-3	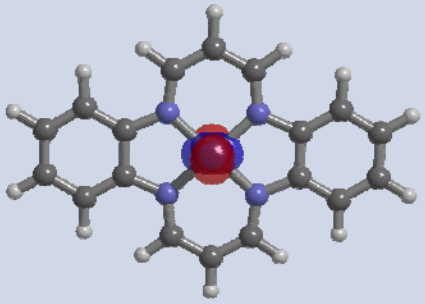 **-6.08**	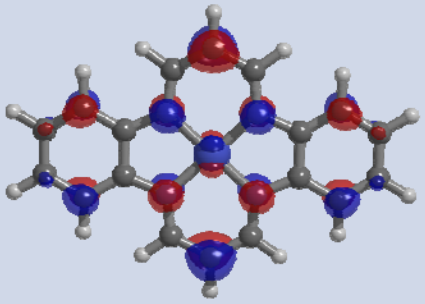 **-5.82**
HOMO-4	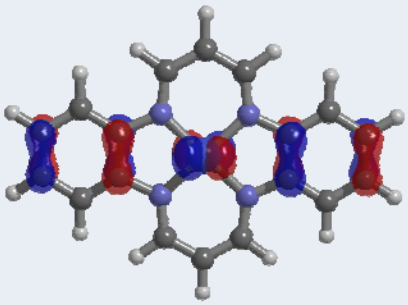 **-6.45**	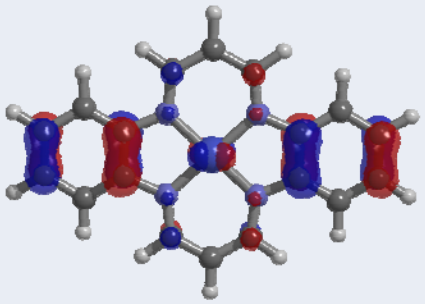 **-6.22**
HOMO-5	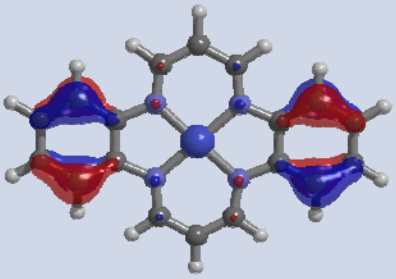 **-6.59**	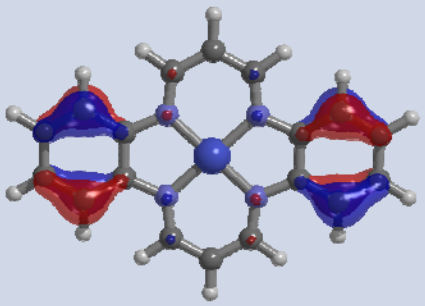 **-6.58**

HOMO-6	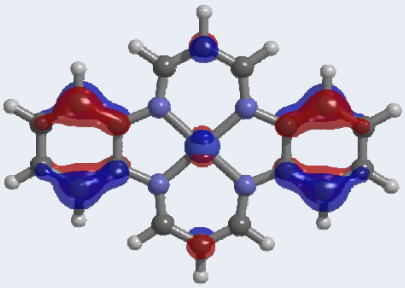 **-7.14**	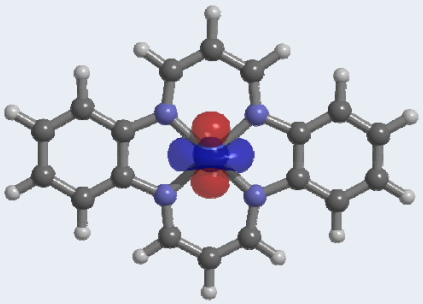 **-6.86**
Spin density	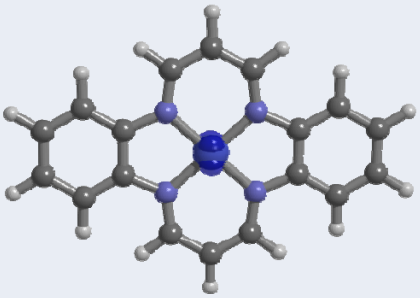	

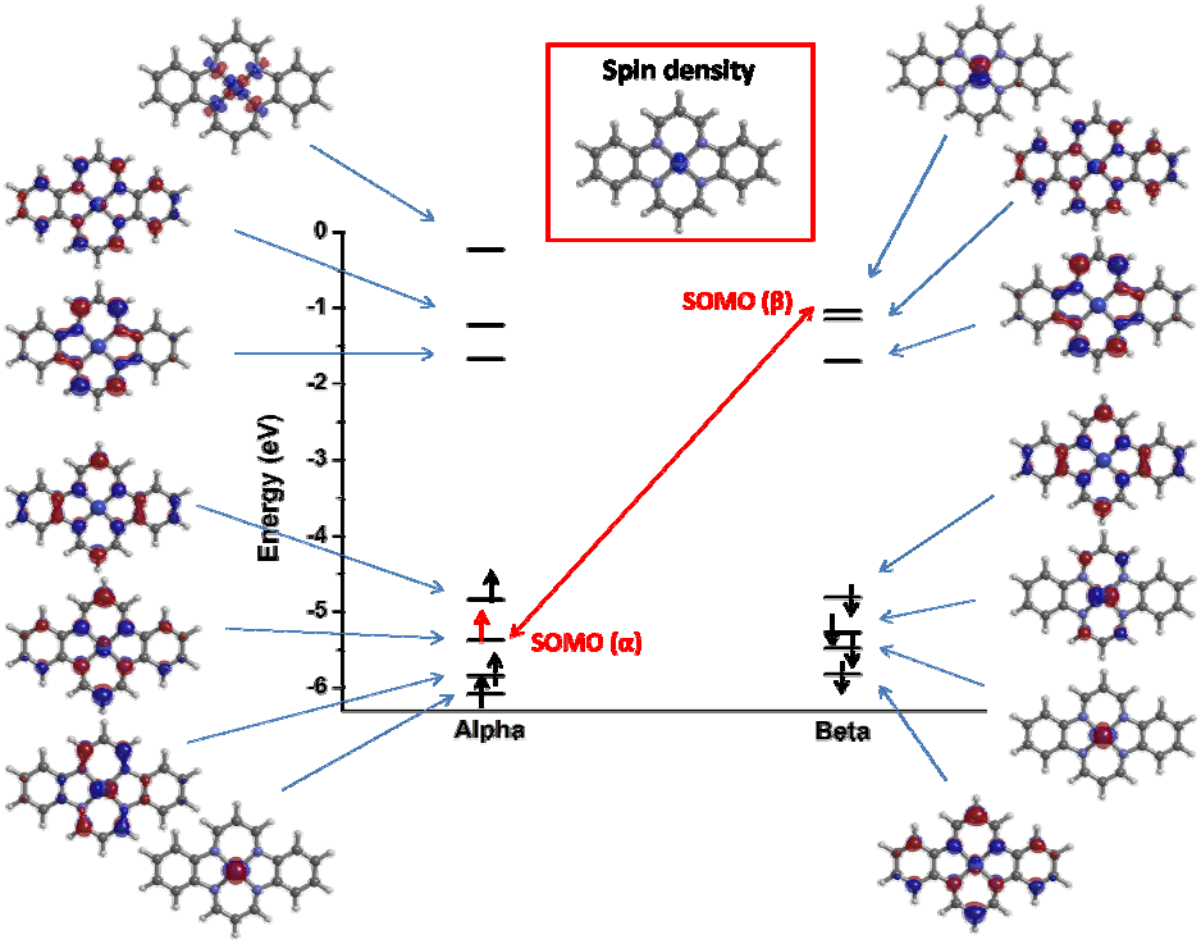

Figure S20 Orbital energies of the alpha and beta orbitals of Co(L1). Also displayed is the calculated spin density.

Table S5 Cu(L1) orbitals and energies from single point calculations at the B3LYP/6-31G(d,p) level of theory.

Orbital	Alpha electron	Beta electron
LUMO+2	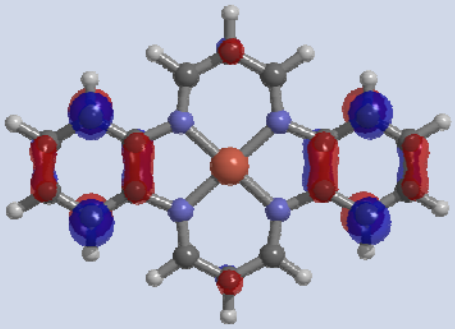 -0.07	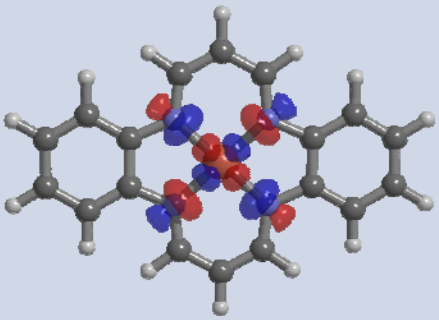 -0.80

LUMO+1	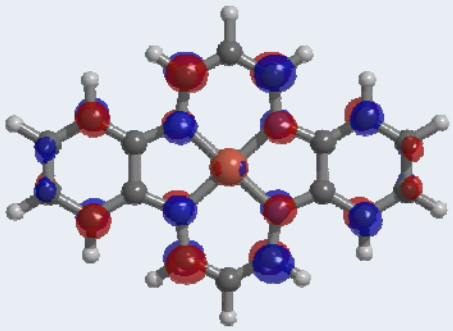 **-1.34**	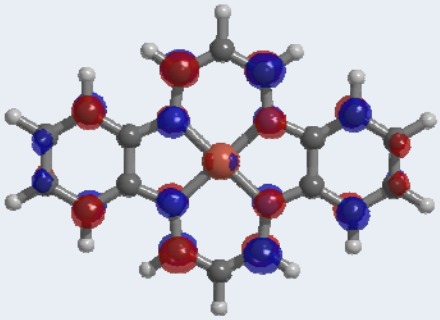 **-1.30**
LUMO	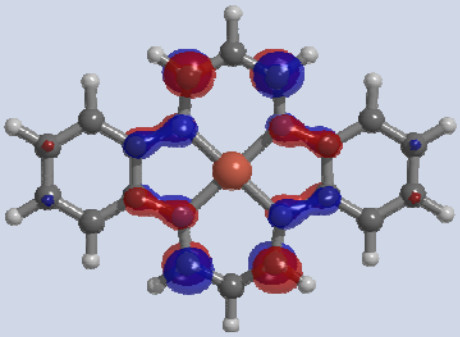 **-1.66**	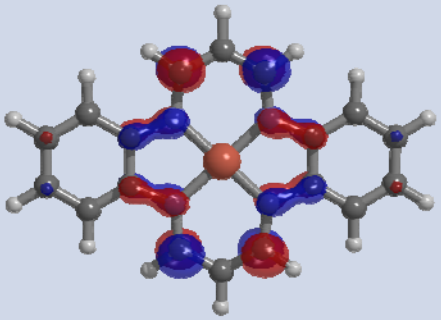 **-1.65**
HOMO	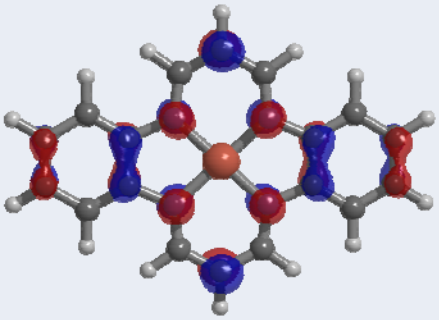 **-4.82**	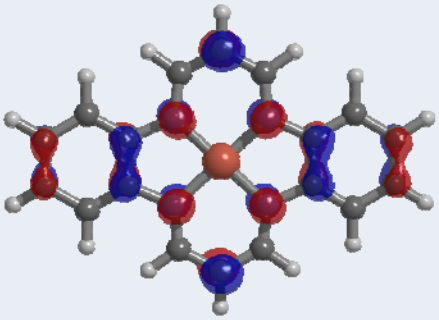 **-4.78**
HOMO-1	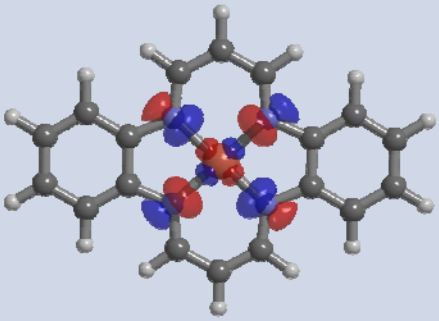 **-4.89**	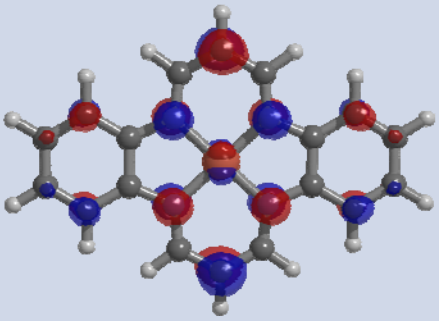 **-5.34**

HOMO-2	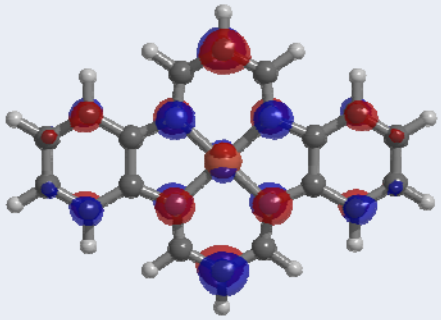 **-5.43**	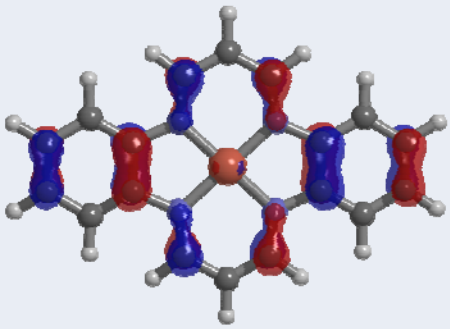 **-6.04**
HOMO-3	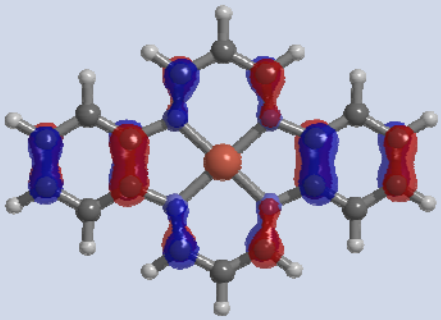 **-6.05**	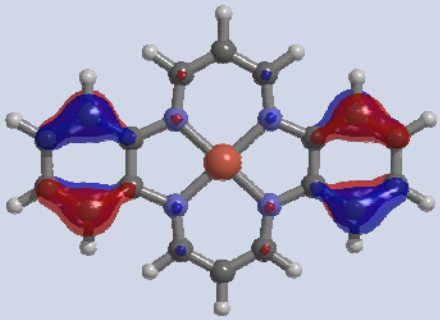 **-6.53**
HOMO-4	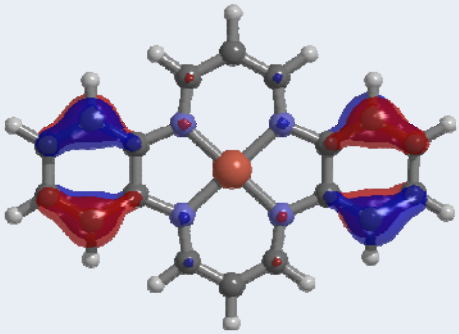 **-6.54**	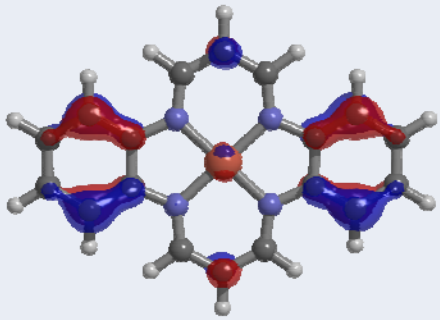 **-7.10**
HOMO-5	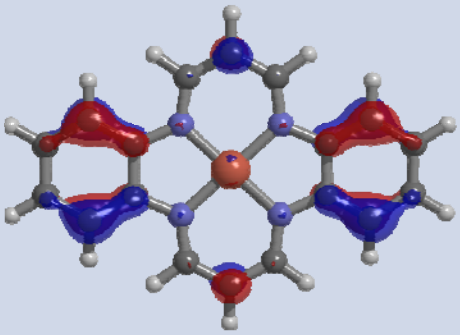 **-7.12**	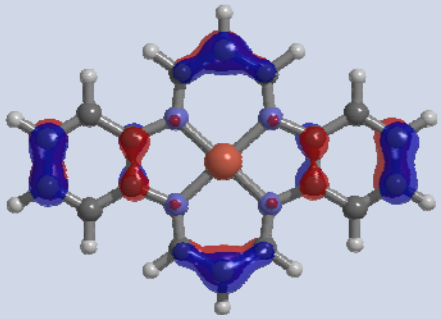 **-7.52**

HOMO-6	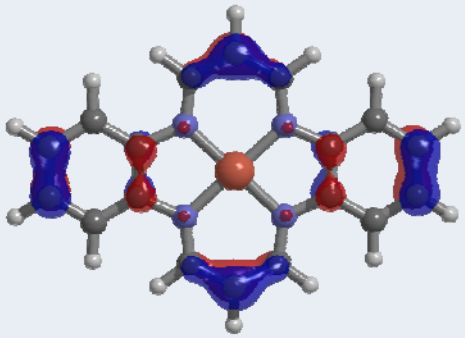 **-7.52**	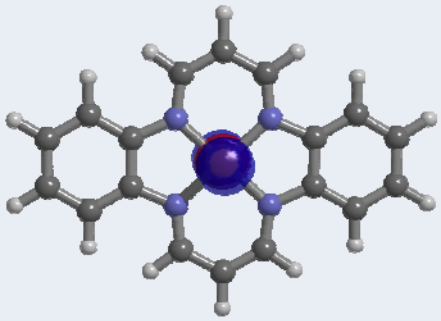 **-7.60**
Spin density	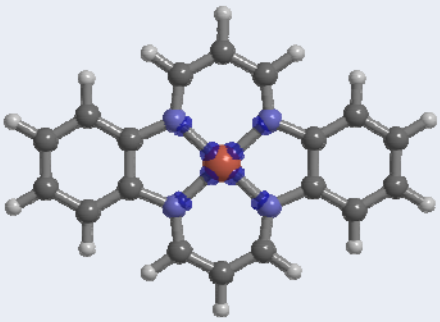	

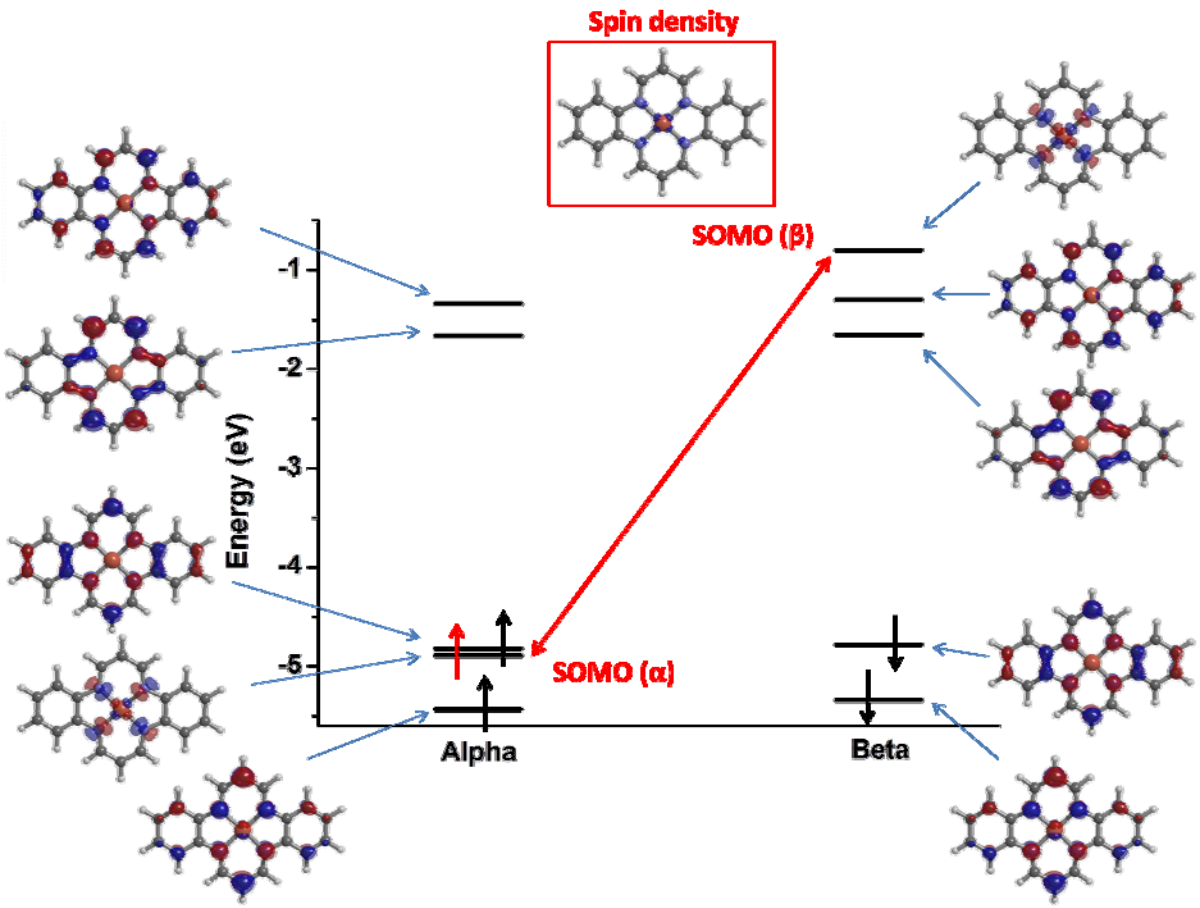

Figure S21 Cu(L1) calculation at the B3LYP/6-31G(d,p) level of theory showing the energies of the frontier orbitals and the spin density.

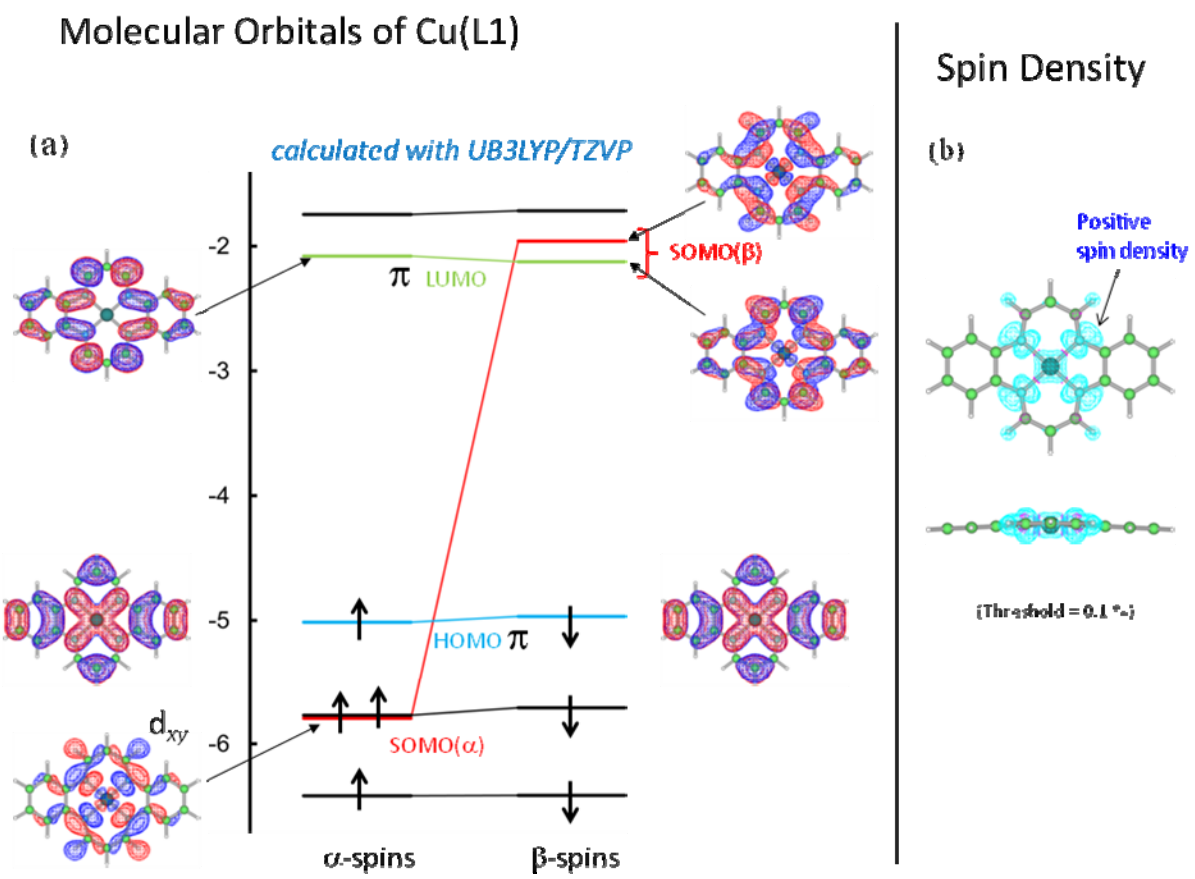

Figure S22 Cu(L1) calculation at the UB3LYP/TZVP level of theory showing the energies of the frontier orbitals and the spin density.

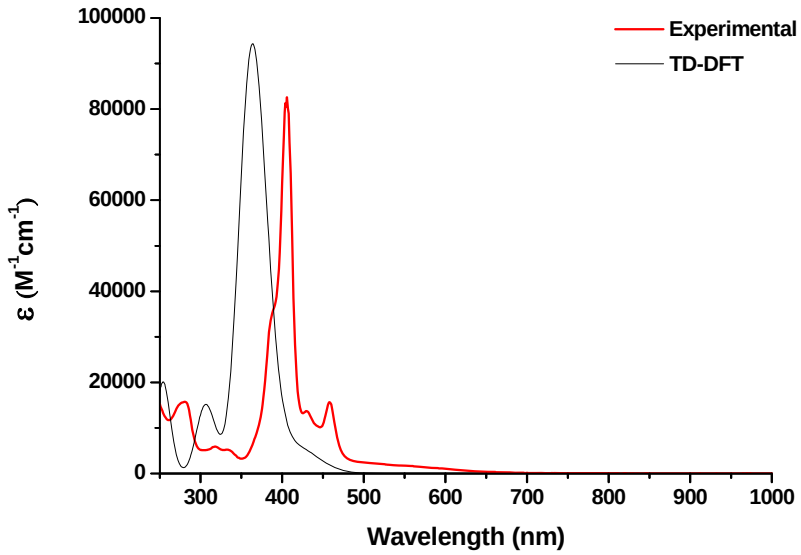

Figure S23 TD-DFT generated absorption spectra overlaid with an experimental solution measurement of Cu(L1).

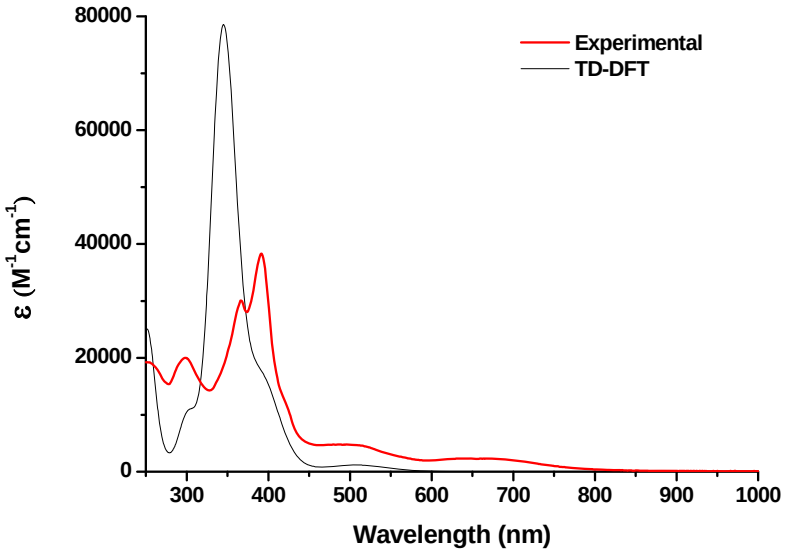

Figure S24 TD-DFT generated absorption spectra overlaid with an experimental solution measurement of Co(L1).

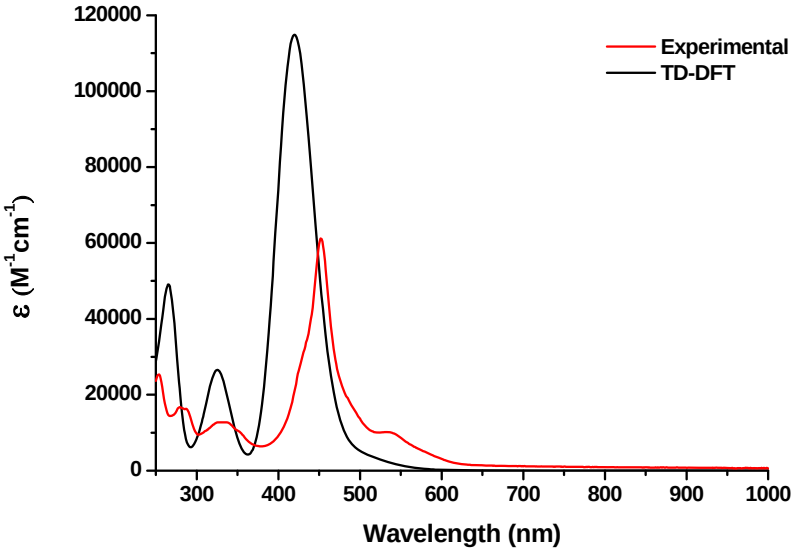

Figure S25 TD-DFT generated absorption spectra overlaid with an experimental solution measurement of Ni(L2).

Table S6 TD-DFT assignment of electronic absorption spectra between 250 and 1000 nm.

Sample	Absorption peak (nm)	Oscillator strength	Major contribution
Co(L1)	393	0.1869	HOMO(A)->L+1(A) (12%), H-3(B)->LUMO(B) (32%), HOMO(B)->L+1(B) (53%)
	345	1.0341	H-1(A)->LUMO(A) (11%), HOMO(A)->L+1(A) (13%),

			H-3(B)->LUMO(B) (51%)
	301	0.1326	H-4(A)->LUMO(A) (33%), H-2(A)->LUMO(A) (12%), H-4(B)->LUMO(B) (36%)
	254	0.1033	H-5(A)->L+1(A) (13%), HOMO(A)->L+4(A) (13%), H-5(B)->L+1(B) (34%), HOMO(B)->L+5(B) (25%)
Cu(L1)	363	1.3016	H-2(A)->LUMO(A) (29%), HOMO(A)->L+1(A) (12%), H-1(B)->LUMO(B) (22%), HOMO(B)->L+1(B) (15%
	306	0.1568	H-3(A)->LUMO(A) (34%), H-2(B)->LUMO(B) (32%), HOMO(B)->L+4(B) (18%)
	254	0.2348	H-2(A)->L+2(A) (17%), HOMO(A)->L+3(A) (27%), H-1(B)->L+3(B) (11%), HOMO(B)->L+4(B) (30%)
Ni(L1)	387	0.8806	HOMO->L+1 (72%)
	335	0.1242	H-4->LUMO (30%), H-3->LUMO (61%)
	302	0.1054	H-4->LUMO (68%), H-3->LUMO (24%)
	290	0.3781	H-6->LUMO (93%)
	252	0.1716	H-5->L+1 (33%), HOMO->L+4 (52%)
Ni(L2)	419	1.5829	H-1->LUMO (67%), HOMO->L+1 (10%)
	324	0.1947	H-5->L+1 (81%)
	267	0.5292	H-7->L+1 (35%), HOMO->L+6 (46%)

† Only transitions between 250 and 1000 nm with an oscillator strength ≥0.1 have been included.

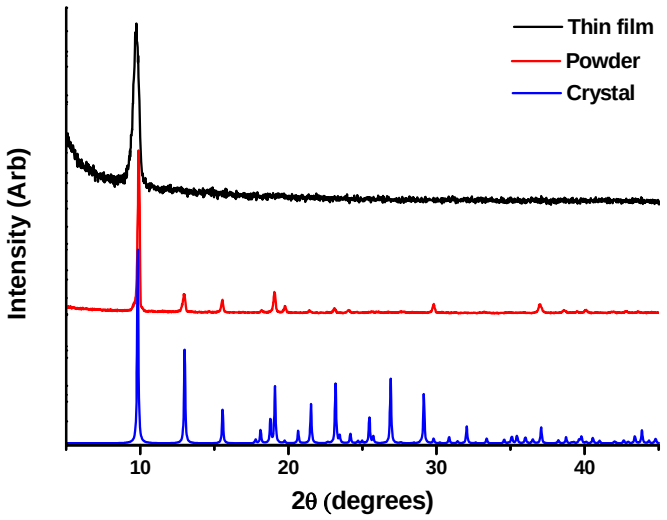

Figure S26 Thin film diffraction pattern of Co(L1) in black, overlaid with the powder pattern in red and single crystal generated pattern in blue.

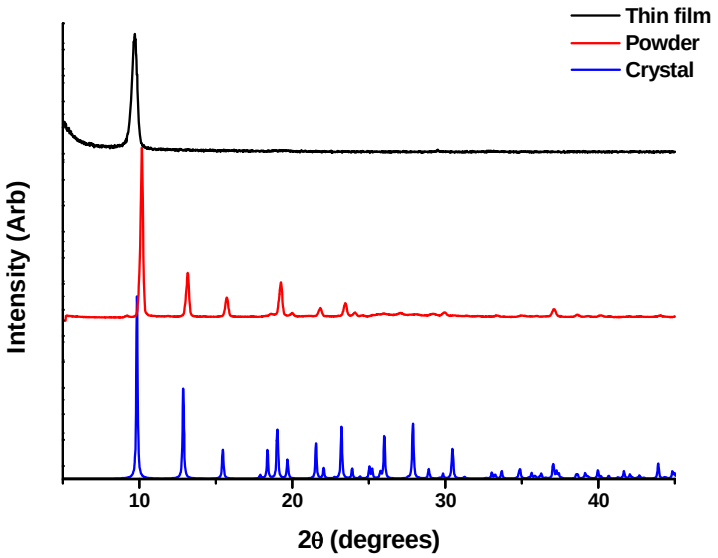

Figure S27 Thin film diffraction pattern of Cu(L1) in black, overlaid with the powder pattern in red and single crystal generated pattern in blue.

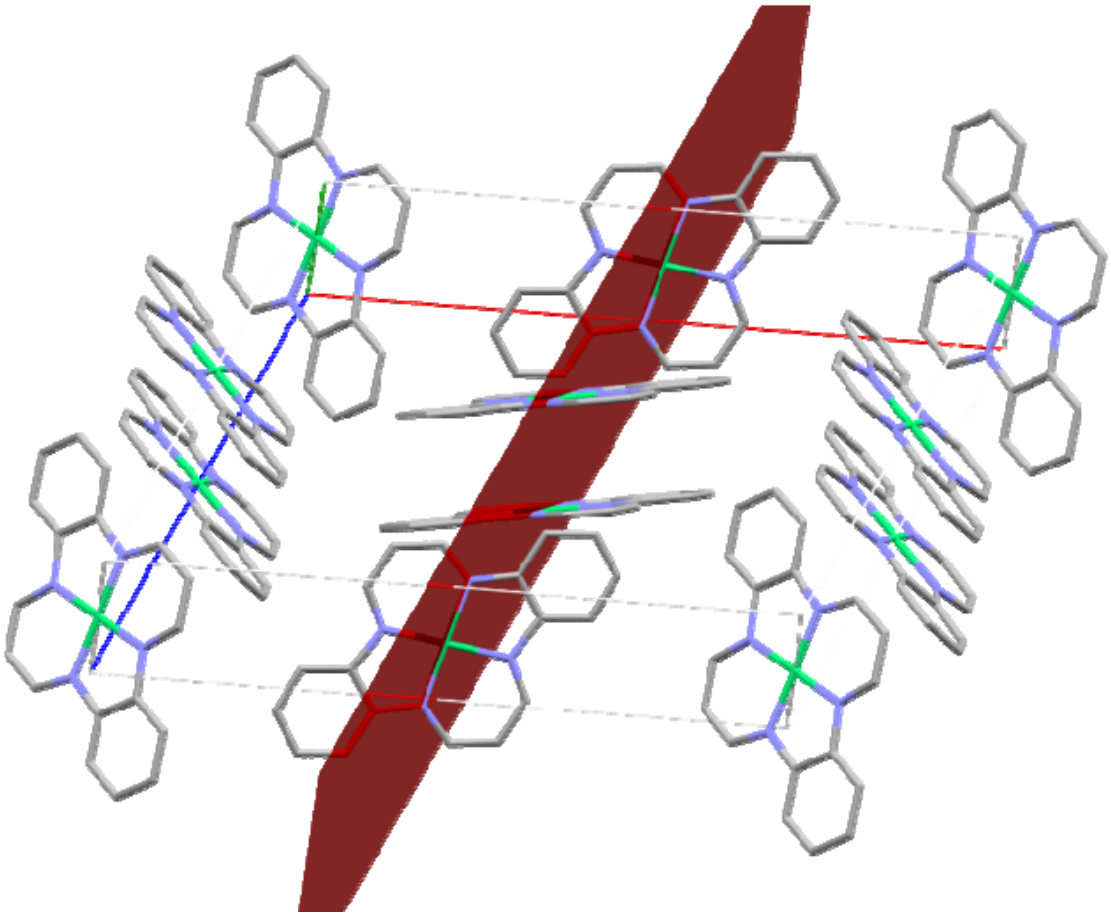

Figure S28 Unit cell of Ni(L1) with the (200) plane highlighted in red.

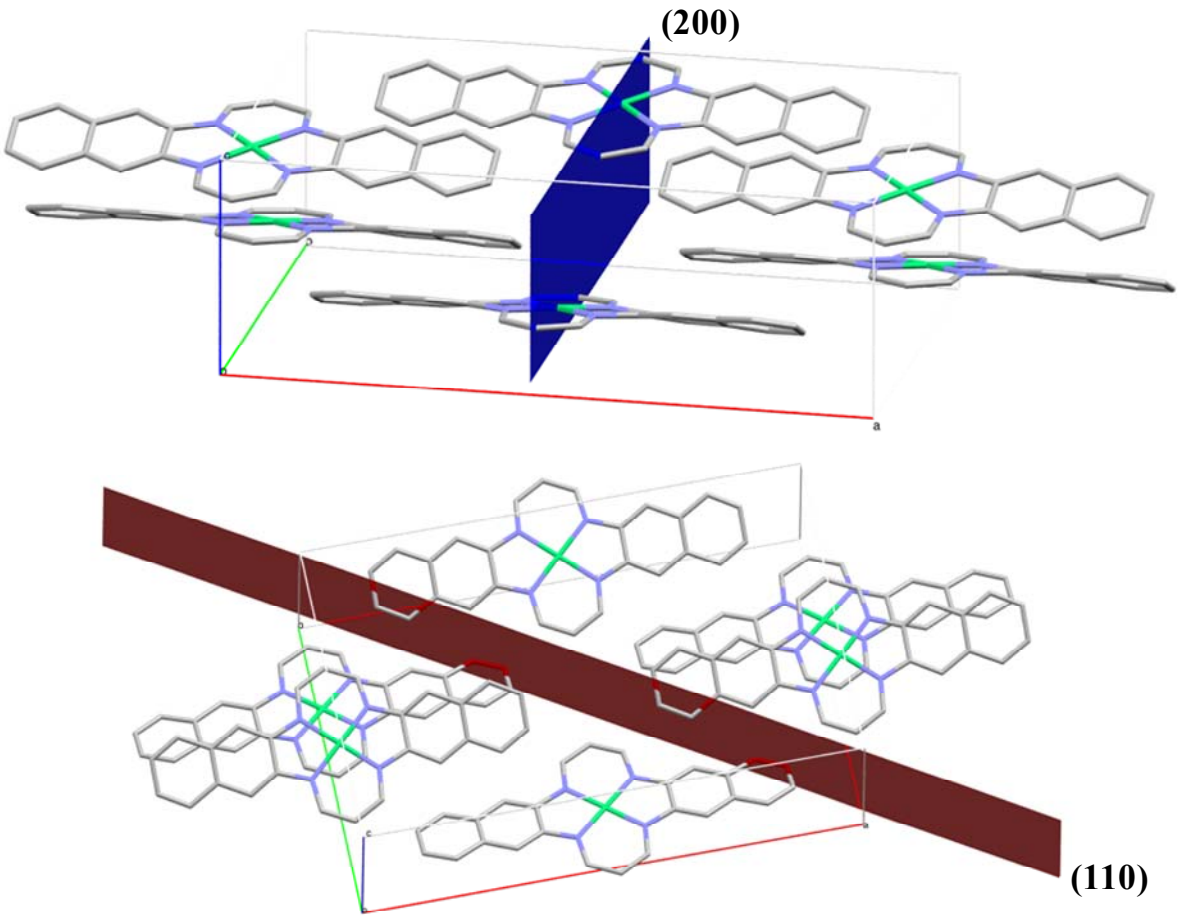

Figure S29 Possible reflections from Ni(L2) thin film XRD.

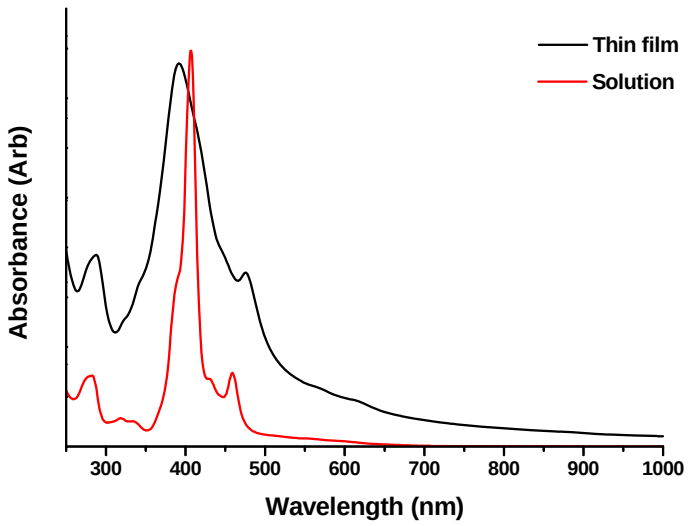

Figure S30 Thin film absorption of Cu(L1) with solution spectrum overlaid.

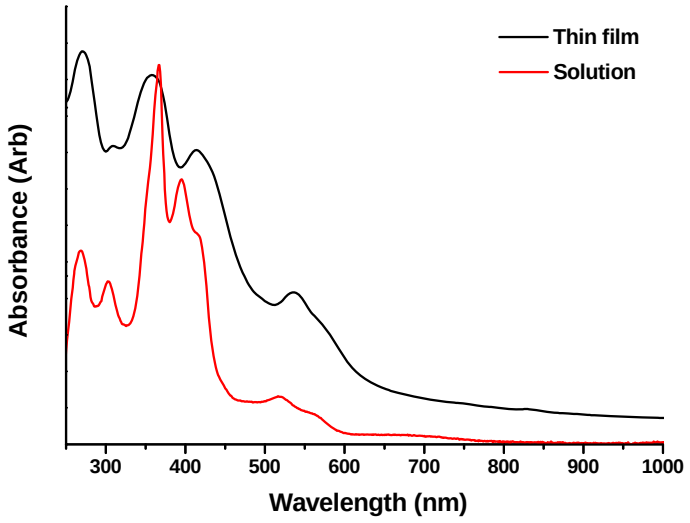

Figure S31 Thin film absorption of Co(L1) with solution spectrum overlaid.

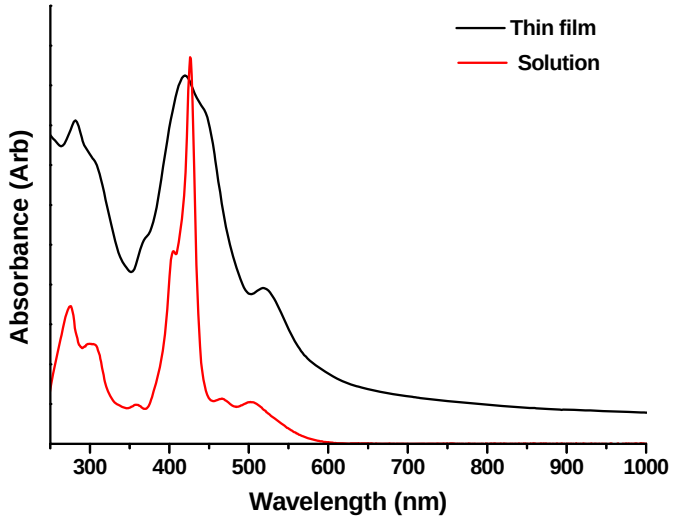

Figure S32 Thin film absorption of Ni(L1) with solution spectrum overlaid.

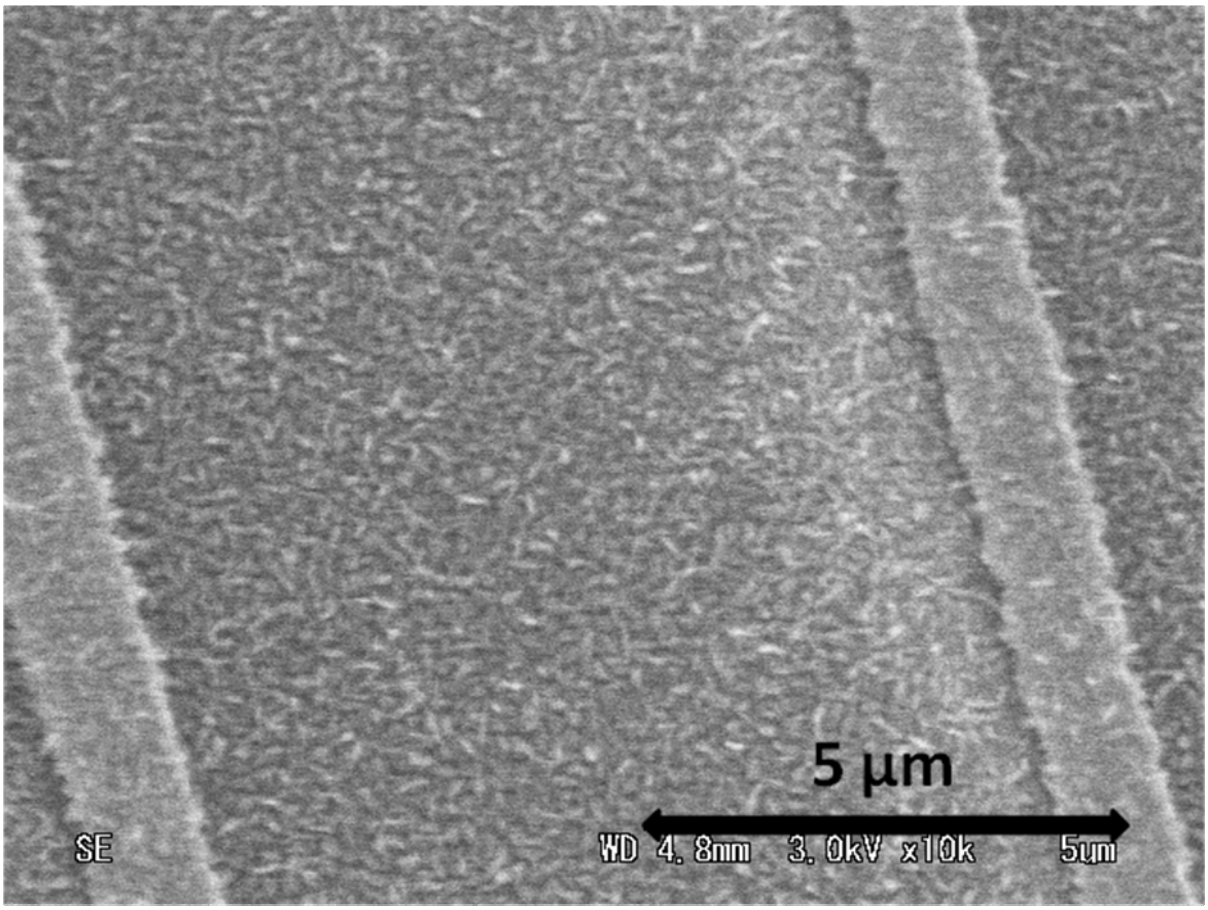

Figure S33 SEM image of Ni(L2).

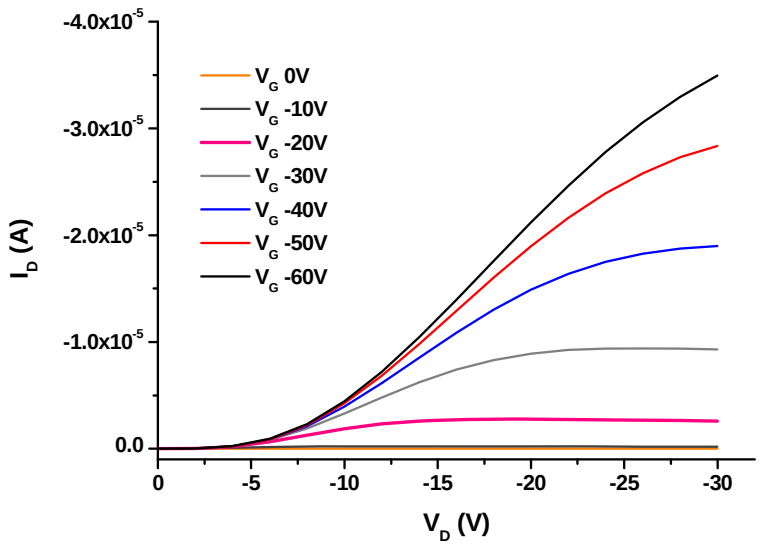

Figure S34 Output characteristics of Ni(L1) on 2x2 µm substrates.

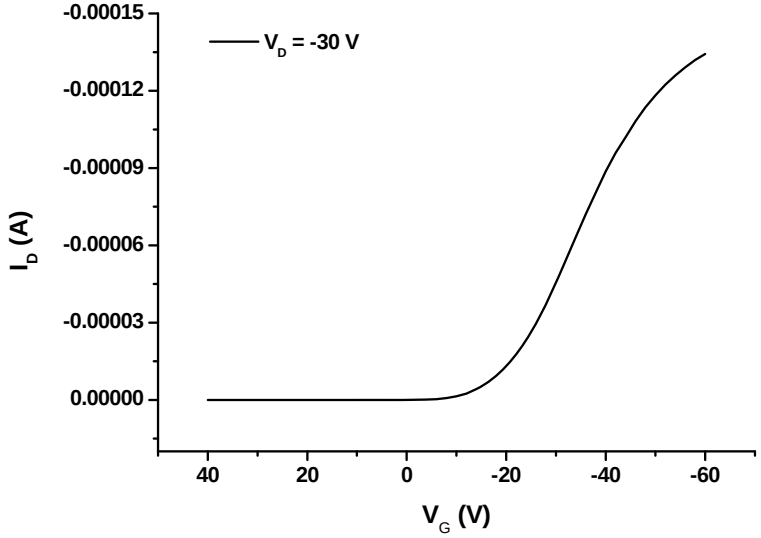

Figure S35 Transfer characteristics of Ni(L1) on 2x2 μm substrates.

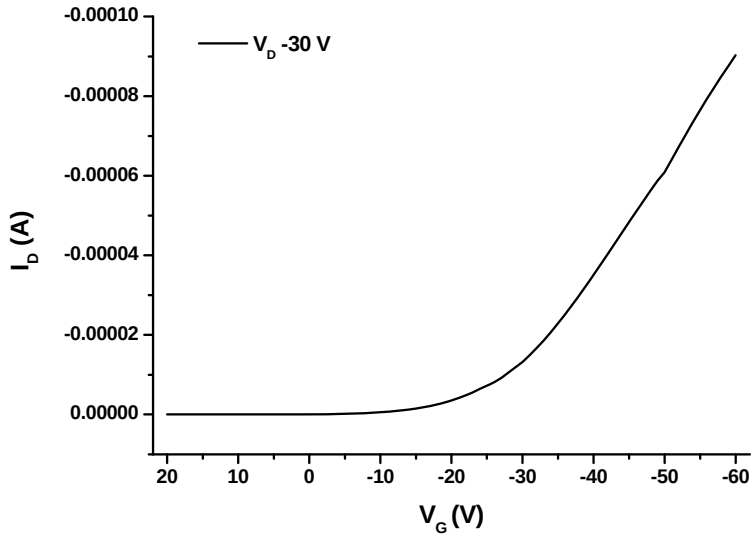

Figure S36 Transfer characteristics of Cu(L1) on 2x2 μm substrates.

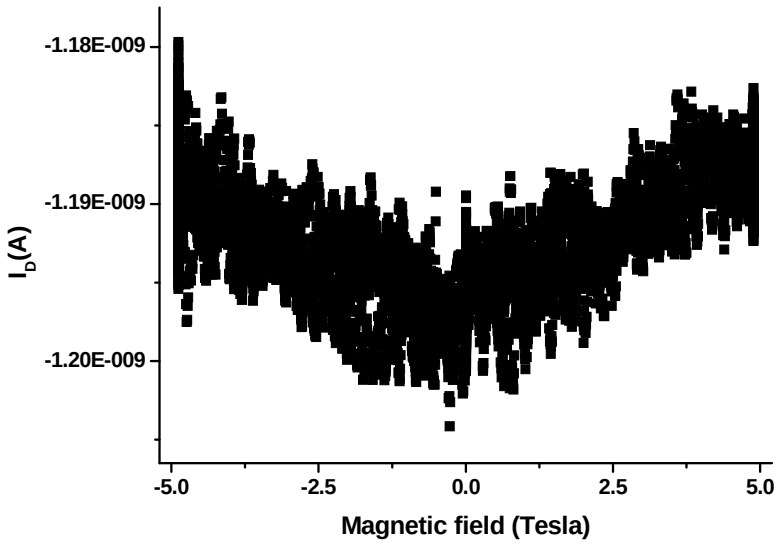

Figure S37 Magnetoresistance measurement on Cu(L1) at 4.35 K when applying a gate voltage of -60 V and a drain voltage of -40 V.

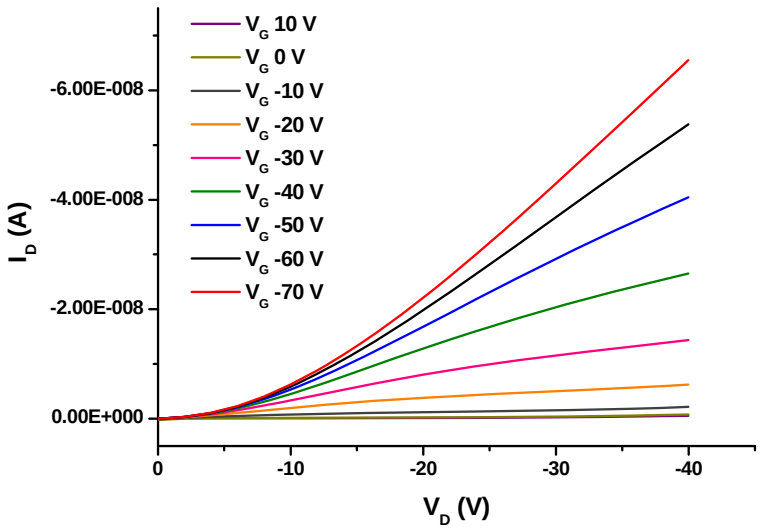

Figure S38 Output characteristics of Co(L1) on 2x2 μm substrates.

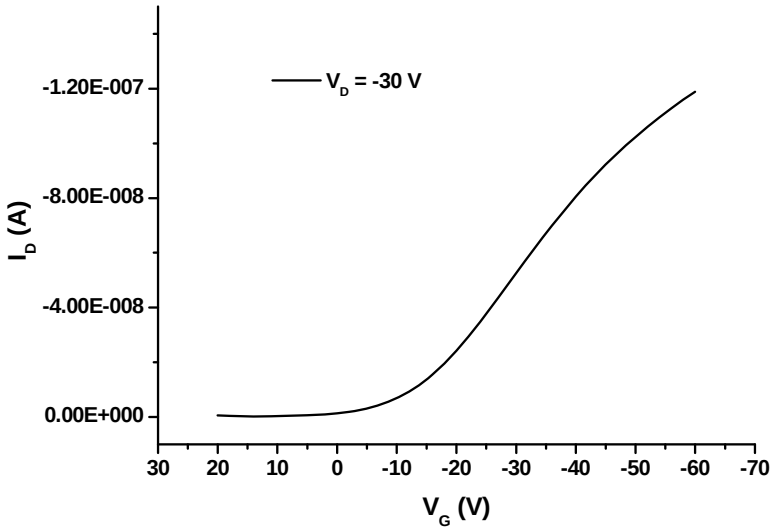

Figure S39 Transfer characteristics of Co(L1) on 2x2 μm substrates.

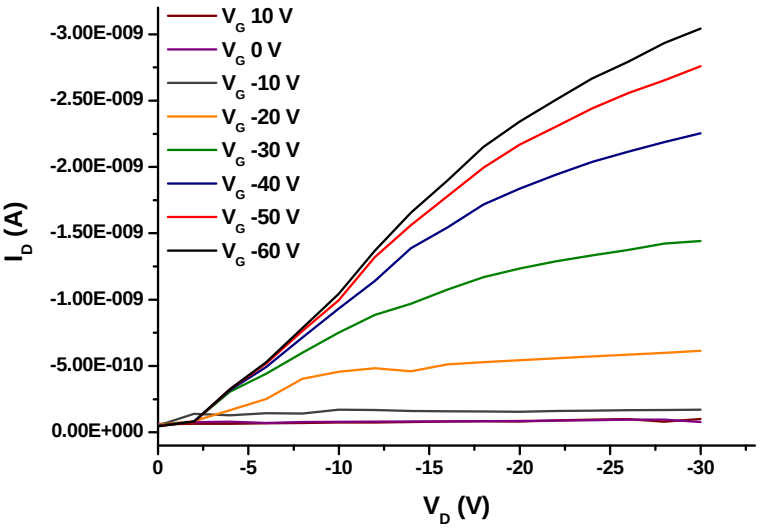

Figure S40 Output characteristics of Ni(L2) on 2x2 μm substrates.

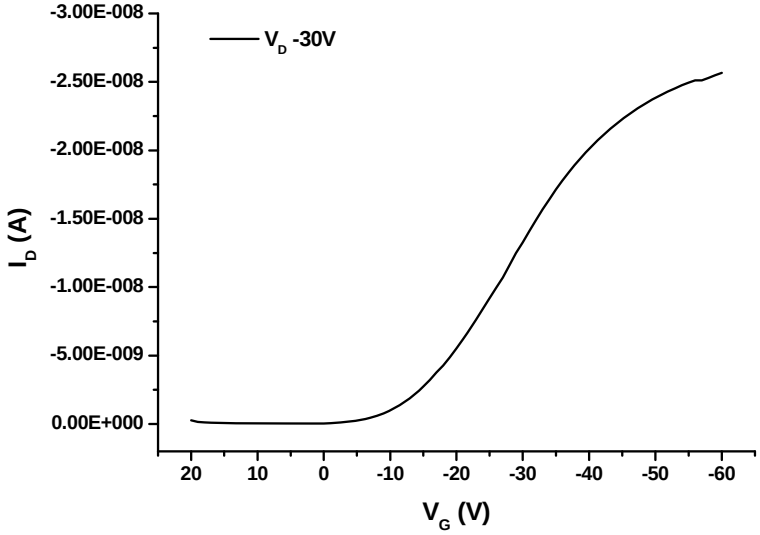

Figure S41 Transfer characteristics of Ni(L2) on 2x2 μm substrates.